Mechanics of Materials 82 (2015) 78–90

Contents lists available at ScienceDirect

Mechanics of Materials

journal homepage: www.elsevier.com/locate/mechmat

Residual stresses due to foreign object damage in laser-shock peened aerofoils: Simulation and measurement

B. Lin [a], S. Zabeen [b], J. Tong [a,*], M. Preuss [b], P.J. Withers [b]

[a] Mechanical Behaviour of Materials, School of Engineering, University of Portsmouth, Portsmouth PO1 3DJ, UK
[b] School of Materials, University of Manchester, Grosvenor St, Manchester M13 9PL, UK

ARTICLE INFO

Article history:
Received 1 July 2014
Received in revised form 2 December 2014
Available online 30 December 2014

Keywords:
Laser shock peening
Foreign object damage
Synchrotron X-ray diffraction
Finite element modelling
Residual stress
Strain map

ABSTRACT

Foreign object damage (FOD) to the leading edge of aerofoils has been identified as one of the main life-limiting factors for aeroengine compressor blades. Laser-shock peening (LSP) has been proposed as a means of increasing the material's resistance to such impact damage. In this work, a three-dimensional finite element (FE) model has been developed to simulate the residual stresses due to head on (0°) and 45° impacts by a cuboidal projectile on aerofoil specimens treated with LSP. The Johnson–Cook (JC) material model was employed to describe the strain rate-dependent material behaviour; whilst the Johnson–Cook dynamic failure model was considered in 45° FOD simulation, where significant loss of material occurred. The strain rate sensitivity of the model at selected high strain rates was assessed against the data from the literature. The numerical results from the simulation of head-on impact were compared with the measurements by depth-resolved synchrotron X-ray diffraction on the mid-plane. The models were then used to predict the 3D residual stress distributions due to 0° and 45° FOD impacts, and the results were compared with the strain maps obtained from high-energy synchrotron X-ray diffraction. Good to excellent correlations between the simulations and the measurements have been found.

1. Introduction

Laser shock peening (LSP) is an advanced surface treatment technique used to introduce compressive stresses to inhibit fatigue crack formation and growth hence enhancing fatigue life as well as the strength of metallic materials (Clauer and Koucky, 1991; Montross et al., 2002; Peyre et al., 1996; Yang et al., 2001). In a LSP process, high-power laser pulses are applied to introduce compressive stresses that extend in millimeter dimensions into thick components (King et al., 2006) or introduce through-thickness compression with balancing tension laterally for thin samples (Rankin and Hill, 2003). Compared with shot peening, compressive residual stresses introduced by LSP can extend to a much greater depth (Montross et al., 2002), for example, to depths in excess of 1 mm for nickel alloy Inconel 718 (Hammersley et al., 2000) and 2 mm in 304 stainless steel (Turski et al., 2010). Titanium alloy Ti–6Al–4V is the focus of the present studies since it is widely used for turbine fan and compressor blades in aircraft engines. The use of LSP has been proposed to treat leading edges of the blades against foreign object damage (FOD) without harming the surface finish (Mannava et al., 1997; Ruschau et al., 1999). Several experimental studies have demonstrated that, due to compressive residual stresses generated in the critical region, laser peened specimens of Ti–6Al–4V alloy exhibited significantly higher fatigue strength than unprocessed ones, including fan blades with a notch or after receiving simulated FOD (Ruschau et al., 1999), plates (Zhang et al., 2010) and cylindrical bars (Altenberger et al., 2012).

* Corresponding author. Tel.: +44 (0)23 982842326; fax: +44 (0)23 92842351.
E-mail address: jie.tong@port.ac.uk (J. Tong).

http://dx.doi.org/10.1016/j.mechmat.2014.12.001
0167-6636/

During landing or takeoff of an aircraft, components in gas turbine engines such as fan blades are often subjected to impacts from small hard particle ingestion, usually identified as FOD which can cause significant damage to the leading edges of the blades (Nicholas et al., 1980). Under service loading conditions, including low-cycle fatigue (LCF), high-cycle fatigue (HCF) and combined LCF and HCF loading, damage induced by FOD can lead to premature fatigue crack initiation and propagation, ultimately causes unexpected fatigue failures in critical engine components (Ritchie et al., 1999; Peters et al., 2000). Several experimental investigations (Ruschau et al., 2001, 2003; Martinez et al., 2002) have been conducted to characterise the influence of FOD for selected impact angles, on the fatigue life of Ti–6Al–4V specimens with a leading edge. From these investigations the effects of FOD on fatigue life have been quantified based on the distribution of residual stresses around the impact notch, the impact angle and the impact damage sustained by measuring the notch depth, loss of material at the notch, material shear, material folding over the leading edge and microstructural damage.

A number of finite element (FE) models have been developed in the past decade to explore the distribution of residual stresses and deformation zones introduced by FOD. One of the main challenges in FE modelling is the choice of a material constitutive model capable of describing material response at very high strain rates experienced during FOD impacts up to $\sim 10^6\,s^{-1}$. Duo et al. (2007) numerically simulated the residual stresses after FOD on the leading edge of Ti–6Al–4V blades. In their simulations, a cuboidal projectile was shot at an inclined angle relative to the axis of the leading edge. The Bammann damage material model was selected and the material constants were obtained from dynamic tests performed at a strain rate of $10^3\,s^{-1}$, and the values of the material constants were numerically extrapolated to higher strain rates. They found that the predicted residual stresses were approximately twice as large as the experimentally measured values. One possible reason for this discrepancy was attributed to the material model in reproducing the strain softening at high strain rates. Boyce et al. (2001) carried out FE simulations of head-on impacts of a sphere on a plate of Ti–6Al–4V alloy. In their studies, an elastic-perfectly plastic material model was used, in which the strain rate sensitivity expressed in a power-law form was included but the effect of strain hardening was neglected. The predicted heights of the notch depth and material pile up were found to match the experimental values well, but discrepancies were observed between the simulated and experimental residual stresses. Frankel et al. (2012) applied the Johnson–Cook material model to simulate the residual stress fields after head-on impact on flat and aerofoil-shaped leading edges, also found the predicted stresses to be approximately twice those measured. The over-estimation of the stresses in their case was attributed to damage at the FOD site, or to the fact that the material constants in the Johnson–Cook model were taken from torsional experiments at strain rates less than $600\,s^{-1}$ (Khan et al., 2004).

All of the above numerical studies examined the residual stresses due to FOD in previously stress-free specimens. However, experimental studies (Ruschau et al., 1999) have demonstrated a significant reduction in fatigue crack growth rates post FOD at low stress ratio in samples previously laser shock peened. Since FOD will cause the redistribution of the residual stresses due to LSP in a component, understanding how FOD affects the residual stress state in components previously treated with LSP is crucial in utilising fully the advantages of LSP in resisting FOD damage susceptible in gas turbine components.

The aim of this study is to simulate FOD impacts head-on (0°) and at 45° directions on previously LSP treated aerofoil specimens, and to compare the results from the simulation with those measured experimentally using high-energy synchrotron X-ray diffraction.

2. Experimental measurement

2.1. Material and specimen

The material is a conventional alloy Ti–6Al–4V which was firstly forged in the α phase and continued into the $\alpha+\beta$ phase, then rolled and creep flattened in the $\alpha+\beta$ phase. The specimens were machined from the forgings similar to those used for the production of fan blades. A generic aerofoil geometry, as shown in Fig. 1a, was adopted. The specimens were laser shock peened over the leading edge at the Metal Improvement Company, USA at a power density of 10 GW/cm^2, using a square spot (size 3×3 mm^2), 50% overlap, 200% coverage and a pulse duration of 27 ns, parameters that provided an optimum balance between the induced residual stresses (FOD tolerance) and the acceptable distortion of the leading edge profile. The total LSP'd area measured approximately 66 mm by 6 mm.

2.2. Introduction of FOD

To mimic the FOD damage conditions that might occur in service from ingested particles impacting at high velocities and strain rates, the specimens were impacted ballistically using a steel cubical projectile via a 12 mm bore light compressed gas gun at the Department of Engineering Science, Oxford University, UK. The gas gun was equipped with a 2 l gas cylinder connected to a 2.5 m long sleeved barrel. Hardened steel cubes were manufactured from a steel gauge plate. After machining the cubes were oil-quenched from 800C with no tempering process applied. An average hardness of the cubes was measured as 63 (Rockwell C). The details of the damage simulation technique are described elsewhere (Nowell et al., 2003). To provide a 'worst case' damage scenario, the steel cubes were mounted in a nylon sabot to prevent rotation and to ensure that the steel cubes hit the leading edge of each specimen in the centre of the gauge length, either with edge first or point first. Two impact cases were studied:

(1) A 3.2 mm cube was aimed directly at the leading edge (0° impact), with an impact velocity of 200 m/s. In this case, the cube hit the specimen edge first (Fig. 1b), and a FOD notch depth around 1.5 mm was introduced.

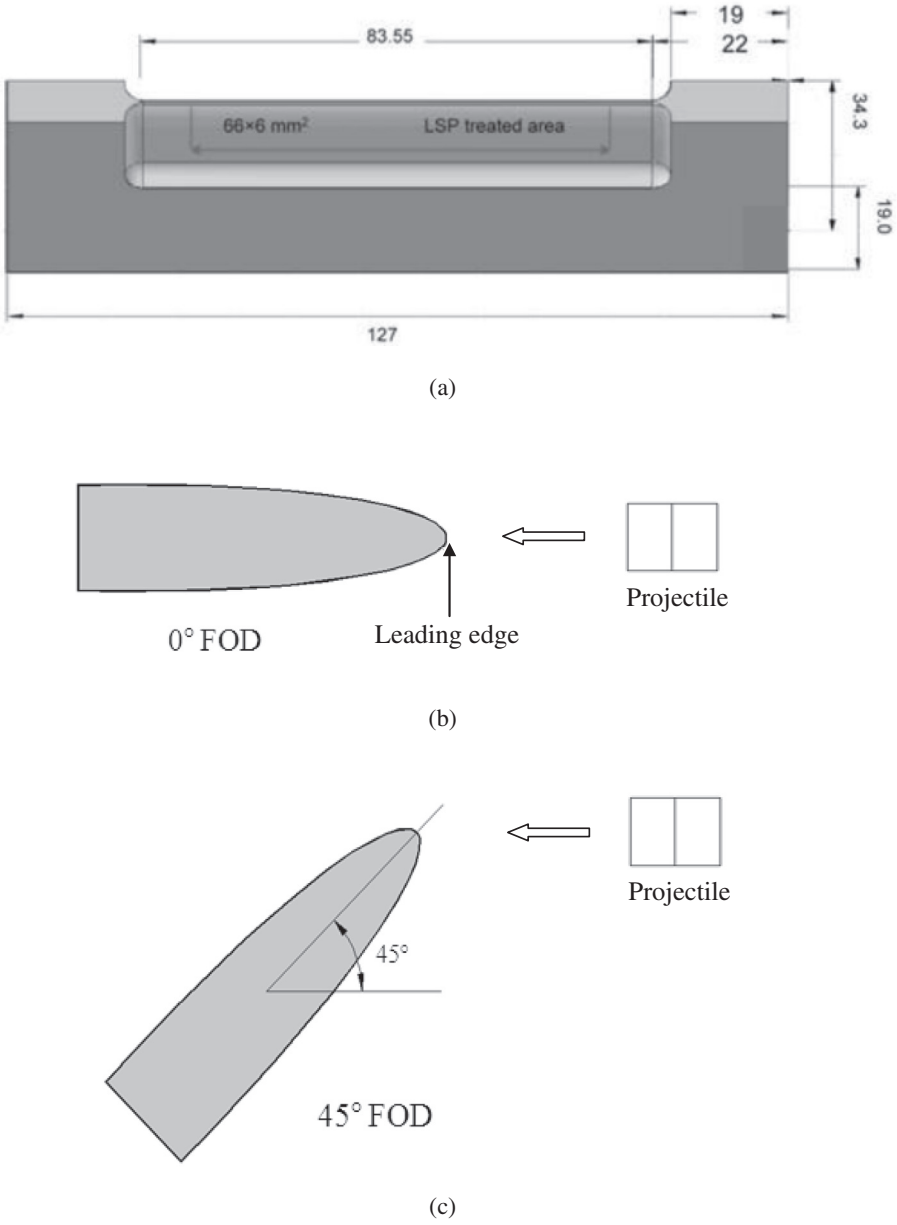

Fig. 1. (a) The geometry of the four-point bend aerofoil specimen (dimensions in mm), and the cross sectional view of the specimen and an illustration of the angle of impact: (b) head-on, (0°); (c) angle impact, (45°).

(2) A 4.8 mm hardened steel cube was directed at an angle of 45° to the leading edge at an impact velocity of 250 m/s. The position of the blade relative to the gun-axis was adjusted in order to achieve the amount of overlap between the cube and the leading edge, so that a depth of approximately 0.75 mm could be obtained (Fig. 1c).

3. Residual stress measurements

Only a brief description of the experimental residual stress measurement method is presented here. Greater detail regarding the experimental technique can be found in (Zabeen et al., 2013). High energy synchrotron X-ray diffraction was carried out on the 1-ID-C beamline at Advanced Photon Science (APS), ANL, Chicago, USA, to measure the through-thickness residual stresses in the as-peened, 0° and 45° FOD impacted specimens (Fig. 2). A monochromatic synchrotron X-ray beam with energy of 65 keV energy (wavelength, $\lambda = 0.1907$ Å) was used. Horizontal and vertical slits were used to define the incoming beam, but no exit slits were employed so that the full thickness of the edge was sampled, resulting in a nominal gauge volume of $0.2 \times 0.2 \times 2$ mm ($x \times z \times y$) (Fig. 1a). The

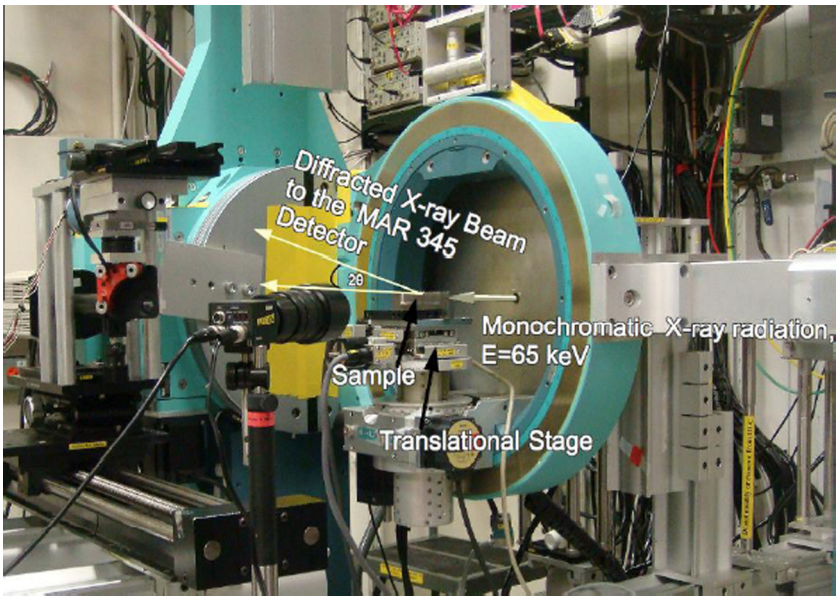

Fig. 2. Through-thickness transmission experiment set up in 1-Id-C beamline at APS, Chicago, USA. The monochromator was selected to choose an energy of 65 keV and a wavelength of 0.1907 Å.

Debye–Scherrer rings were collected on a MAR-345 image plate. The 2D diffraction images were corrected and integrated by a data reduction program, FIT2D (Hammersley et al., 1996) to convert the 2D pixel image to 1D line diffraction spectra. To do this the diffraction rings were integrated over arcs (±10°) centred on 0° and 90°, giving five diffraction peaks that may be fitted. Only the $(10\bar{1}2)$ plane from Ti-α phase was used for this study ($2\theta = 6.6°$). Elastic strains were obtained relative to a strain-free lattice spacing, d_0 measured at a location far away from the peened area (Withers et al., 2007). The strains in the longitudinal (x) and the transverse (y) directions were used to infer the stresses, assuming bi-axial stress state. On an average, 900 individual measurement locations were mapped for each specimen with step-sizes of 0.2 mm and 0.1 mm in the longitudinal and the transverse directions, respectively.

To examine the residual elastic strain variation across the thickness of the specimens, depth-resolved residual elastic strains were measured on ID 31 beamline at the European Synchrotron radiation facilities (ESRF) (Fig. 3).

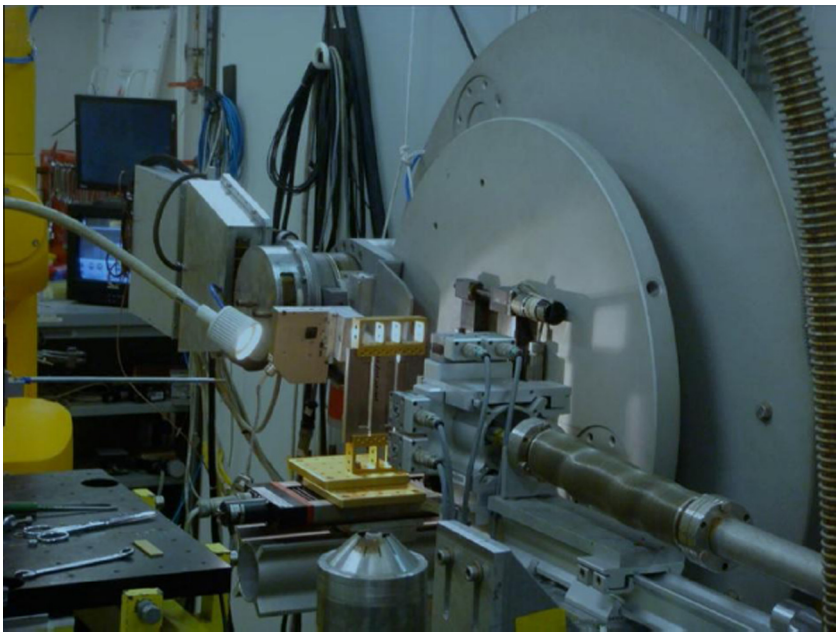

Fig. 3. Experimental arrangement for depth resolved residual elastic strain scanning of aerofoil specimens on Id-31 at ESRF.

A monochromatic synchrotron X-ray beam was selected (50.8 keV, 0.244 Å). The displacement of the diffraction peak from Ti-α phase was measured at a scattering angle (2θ) of 8.2°. The illuminated volume in the specimen was defined by two slits of dimensions 0.4×0.05 mm^2 on the incident and diffracted beam. This resulted in an elongated gauge volume that was 0.9 mm long, 0.4 mm wide and 0.05 high that allowed us to resolve the strain changes with depth (y). To avoid surface artifacts an analyser crystal was used for the diffracted beam (Withers, 2013). A line scan was carried out with a dense (step-size of 0.1 mm) pattern over the first 3 mm from the notch root, thereafter sparsely distributed measurement points were taken. The distribution of diffracted intensity as a function of 2θ was assumed to be a Pseudo-Voigt peak shape and fitted using Large Array Manipulation Program (LAMP) to determine the centre of the peak position and also the full width half maximum (FWHM).

The bulk elastic constant was used to calculate the stresses from the strains. From the literature it has been confirmed that $(10\bar{1}2)$ peak represents the bulk elastic constant of the material. However, along with $(10\bar{1}2)$ diffraction peaks, 101 peak was also analysed at the preliminary stage and found no significant difference between the two sets of results. Therefore the data analysis was processed with $(10\bar{1}2)$ peak.

4. Finite element (FE) modelling

In order to predict the 3D residual stress and elastic strain distributions first introduced by LSP and then modified by FOD, ABAQUS/Standard and Explicit (2012) were used, respectively. Only the blade section of the aerofoil specimen was modelled in the impact simulations to reduce the computational costs without significant loss of accuracy. This was possible due to the significantly increased thickness of the specimen beyond the aerofoil section, so that a fixed boundary condition may be applied to simulate the constraint from the rest of the specimen. Due to symmetry of the blade and considering the loading conditions, a quarter of the specimen for head-on impact and a half of the specimen for 45° impact were considered in the FE models. The 3D FE meshes for the both specimens are shown in Fig. 4a and b. The mid-lines on the symmetry plan are marked by line "mn", and the coordinate system origin is located at point "n". The models were meshed with 8-noded linear brick elements with reduced integration and enhanced hourglass control. Due to negligible plastic deformation experienced during impact (Nowell, 2008), the steel cubical projectile was assumed linear elastic (Young's modulus, 206 GPa, and Poisson's ratio, 0.3), and meshed using 4-node linear tetrahedral elements.

4.1. Introduction of LSP residual stresses into FE model

The residual elastic strains due to the LSP treatment were obtained by depth-resolved synchrotron X-ray diffraction (Zabeen et al., 2013), as described in Section 3. The associated residual stresses in the specimen were calculated from the measured residual elastic strains by

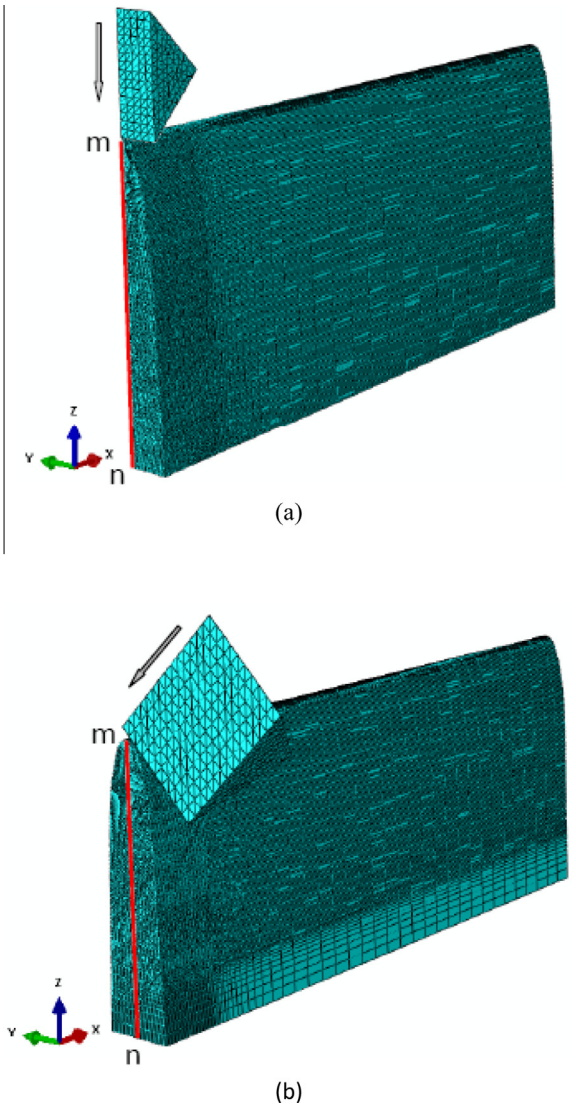

Fig. 4. The 3D finite element model for (a) head-on impact (quarter model); (b) 45° impact (half model). (Arrows indicate the impact direction and mid-line mn is on the symmetric mid-plane).

applying Hooke's law for isotropic materials under 3D conditions. The stress–strain curve of Ti–6Al–4V alloy was described by the Ramberg–Osgood relation at room temperature (MIL-HDBK-5J, 2003). The residual stresses introduced by peening were assumed to be only a function of the z-coordinate (Fig. 5) and inputted into the FE model as initial stresses through the *Sigini* subroutine of ABAQUS/Standard (2012). It is interesting to note that the laser peening in this case has introduced an essentially uniaxial stress parallel to the leading edge that varies with distance with the leading edge. In order to match the residual stresses to the measured values, an iterative scheme with a proportional integral adjustment (Lei et al., 2000) was applied with the adjustment equation:

$$\sigma(x)^{i+1}_{inp} = \sigma(x)^{i}_{inp} + \beta\left(\sigma(x)_{targ} - \sigma(x)^{i}_{out}\right) \quad (1)$$

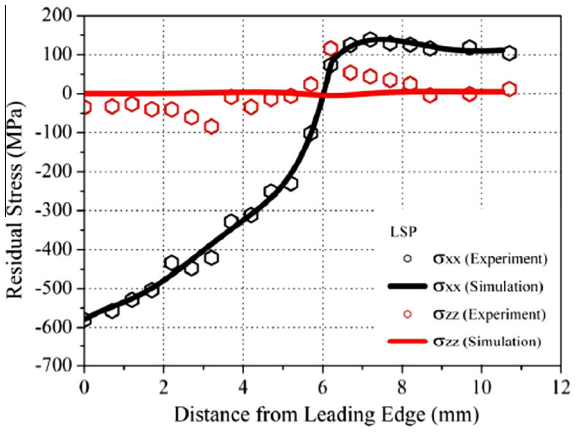

Fig. 5. Comparison of the experimentally measured residual stresses due to LSP on mid-line mn and those introduced by iteration in the FE model.

where $\sigma(x)_{inp}^{i+1}$ and $\sigma(x)_{inp}^{i}$ are the input values of stress for the $(i+1)$th and ith iterations respectively, β is the integral factor (taken to be 1 here), $\sigma(x)_{targ}$ is the target stress value and $\sigma(x)_{out}^{i}$ is the stress value obtained as the output of the ith iteration. The procedure started with $i=0$ and $\sigma(x)_{inp} = \sigma(x)_{targ}$. The value of $\sigma(x)_{out}$ was then obtained from the FE analyses, $\sigma(x)_{inp}$ was calculated using Eq. (1) for the next iteration and so on until $\sigma(x)_{out}^{i}$ became equal to $\sigma(x)_{targ}$. Using this iterative process the initial residual stresses were well simulated by the model, as shown in Fig. 5. There is some discrepancy for σ_{zz} between the inputted and the target values, although compared with σ_{xx}, σ_{zz} is much smaller in magnitude, hence its influence on subsequent stress states, particularly the x component, may be insignificant.

4.2. FOD simulation

4.2.1. Material model and parameter determination

The Johnson–Cook constitutive relation and the associated failure criterion were adopted in this work, following the most recent work of Wang and Shi (2013) who reported a good agreement between the experimental results and the FE predictions of the dynamic response of Ti–6Al–4V alloy under high-speed impact at various velocities and angles. The Johnson–Cook constitutive model is given by Johnson and Cook (1983, 1985):

$$\sigma_y = (A + B\varepsilon^n)\left[1 + C\ln\left(\frac{\dot{\varepsilon}}{\dot{\varepsilon}_0}\right)\right]\left[1 - \left(\frac{T - T_r}{T_m - T_r}\right)^m\right] \tag{2}$$

where σ_y is the flow stress of the material; A, B, n, C and m are experimentally determined constants: A is the initial yield strength, B and n represent the effects of strain hardening, C is the strain rate sensitivity coefficient and m is the thermal softening coefficient. The equivalent plastic strain, the equivalent plastic strain rate measured at or below the transition temperature are denoted as $\varepsilon, \dot{\varepsilon}$ and $\dot{\varepsilon}_0$, respectively; T, T_γ and T_m are current, transition and melting temperatures.

There are some variations in the material constants of the Johnson–Cook constitutive model reported for Ti–6Al–4V alloy (Lesuer, 2000; Meyer and Kleponis, 2001; Hubert and Meyer, 2006), due to the difficulties in experiments at strain rates over $10^3\,s^{-1}$ (Duo et al., 2007), hence constants from the literature were used only as guide values in the initial trials.

A dynamic failure model using the Johnson–Cook shear failure criterion (ABAQUS, 2012) was applied to model the material loss during impacts at 45°. The Johnson–Cook dynamic failure model is based on the value of the equivalent plastic strain at element integration points; whilst failure is assumed to occur when the damage parameter exceeds 1, the failed elements were deleted and removed from FE model automatically, a feature available in ABAQUS. The damage parameter, ω, is defined as:

$$\omega = \sum\left(\frac{\Delta\varepsilon}{\varepsilon_f}\right) \tag{3}$$

where $\Delta\varepsilon$ is an increment of the equivalent plastic strain, ε_f is the strain at failure, and the summation is performed over all increments in the analyses. The strain at failure, ε_f, is assumed to be dependent on a nondimensional plastic strain rate, $\dot{\varepsilon}/\dot{\varepsilon}_0$; a dimensionless pressure-deviatoric stress ratio, p/q (where p is the pressure stress and q is the von Mises stress); and the nondimensional temperature, $(T - T_r)/(T_m - T_r)$, defined above in the Johnson–Cook hardening model. The strain at failure is defined as:

$$\varepsilon_f = \left[d_1 + d_2 exp\left(d_3\frac{p}{q}\right)\right]\left[1 + d_4 ln\left(\frac{\dot{\varepsilon}}{\dot{\varepsilon}_0}\right)\right]\left(1 + d_5\frac{T - T_r}{T_m - T_r}\right) \tag{4}$$

where d_1–d_5 are failure parameters measured at or below the transition temperature, T_r. These failure parameters for Ti–6Al–4V alloy are taken from the literature (Kay, 2003) and are summarized in Table 1.

Our experimental studies of FOD on laser-shock peened Ti–6Al–4V aerofoils (Spanrad and Tong, 2011) have shown that, for head-on impacts, a "V" notch was obtained on the leading edge with typical features of material folding and piling up. By contrast, for 45° impacts, the projectile "sheared off" part of the leading edge during impact, so loss of material is an important feature of 45° impacts. Based on these experimental observations, the Johnson–Cook dynamic failure model was applied in the 45° impact simulations, whilst the Johnson–Cook deformation model was used to simulate the head-on impacts.

4.2.2. Numerical analysis

In order to find an optimum mesh size for the impact simulation, a mesh convergence analysis was carried out.

Table 1
Johnson–Cook (JC) material parameters for Ti–6Al–4V.

A (MPa)	B (MPa)	n	m	C
JC material constants				
1035	331	0.635	1.7	0.04
d_1	d_2	d_3	d_4	d_5
JC failure parameters (Kay, 2003)				
−0.09	0.27	0.48	0.01	3.87

Three mesh sizes: 0.035, 0.07 and 0.14 mm, were considered in the volume of interest, i.e. potential impact site, in the convergence analysis. An element size of 0.07 mm was deemed sufficient to obtain accurate results without incurring huge computational costs. The frictional effect between the projectile and the Ti–6Al–4V blade was included in the impact simulation using a coulomb law of sliding friction with friction coefficient of 0.3. At the same time, to avoid severe deformation and distortion of elements during the impact simulation, an Arbitrary Lagrangian–Eulerian meshing technique was applied over the region of interest. In addition, heat may be generated by the plastic deformation at high strain-rates, resulting in thermal softening. When deformation occurs rapidly, there is insufficient time for redistribution of the generated heat, so an adiabatic process was adopted in the impact simulation. The impact analyses were conducted on the FE model with the residual stresses due to the LSP prescribed, and simulations of firing a steel cuboidal projectile (2.2) at the target (Fig. 4) were carried out.

4.2.3. Steady-state residual stress

Although ABAQUS/Explicit (2012) provides numerical damping in the form of bulk viscosity to control high frequency oscillations, our analyses showed that steady-state stress state was extremely slow to reach using this approach. Eltobgy et al. (2004) pointed out that the time required to reach the steady state stress was much longer when considering numerical damping, rather than material damping. Hence in the present study material damping was applied to accelerate the dynamic process to a steady state. The magnitude of material damping may be calculated by the following equation (Eltobgy et al., 2004):

$$\alpha = 2\xi\sqrt{(E/\rho)/L_e} \tag{5}$$

where ξ is damping ratio, E is Young's modulus, ρ is material density and L_e is the length of the element.

5. Results and discussion

5.1. Materials parameters

Accurate determination of the material parameters at high strain rates in the Johnson–Cook model is of vital importance for the FE simulations. In this work, we adopted an optimisation procedure to obtain these parameters through iterative FE analyses. The procedure is as follows: The material parameters were calibrated by fitting the residual stress response on the mid-line "mn" in the FE model subjected to heat-on impact, shown in Fig. 4a. Prior to the fitting process, initial material constants were estimated from the literatures (Lesuer, 2000; Meyer and Kleponis, 2001; Hubert and Meyer, 2006). Following each simulation, the resulting residual stress profile σ_{xx} along the mid-line "mn" was compared those measured experimentally at ESRF (Fig. 6), the magnitude of the difference between the two was considered in an objective function over the history. Optimisation was carried out until the error was minimised. The comparison between the experimental and the simulated stress components in X-direction are presented in Fig. 6, together with simulated stress components in Y and Z directions. The capacity of the model prediction of strain rate sensitivity of the material was examined using the experimental data from Hubert and Meyer (2006), and the results are shown in Fig. 7, where a reasonably good agreement is achieved. It seems that the Johnson–Cook model can capture saturated stress at high strain rates over 10^4/s. The final optimised Johnson–Cook material constants used in this study are given in Table 1.

The above Johnson–Cook material constants, together with the Johnson–Cook failure parameters d_1–d_5, taken from Kay (2003, also given in Table 1), were then applied to simulate the 45° FOD impact. The predicted residual stresses σ_{xx}, σ_{yy} and σ_{zz} along the mid-line are given in Fig. 8. It can be seen that the profile of simulated residual stress σ_{xx} along the mid-line agrees well with those measured from the depth-resolved experiment data at ESRF, especially the magnitude and the location of the maximum compressive and tensile residual stresses. However, the critical values close to the notch differ from the experimental results with the predicted stresses around 170 MPa more compressive than the experimental results. This difference might be due to a number of reasons, including the uncertainties in the measurement in areas close to the impact notch, where very high stress gradient presents, or the numerical strategies adapted in the impact simulation. A previous study (Wang and Shi, 2013) on impact damage of the same material showed that, because of the removal of fully damaged elements from the notch in the simulation, the mesh size around the impact region has a substantial influence on the simulation results. Models with a coarse mesh tend to predict more material loss than that predicted by models with a finer mesh, although the mesh sensitivity was tested in the current study.

5.2. Comparison of residual stresses from FE simulation and synchrotron measurement

Comparing the residual stress distribution along the mid-line (Figs. 6 and 8) after FOD with that for the LSP

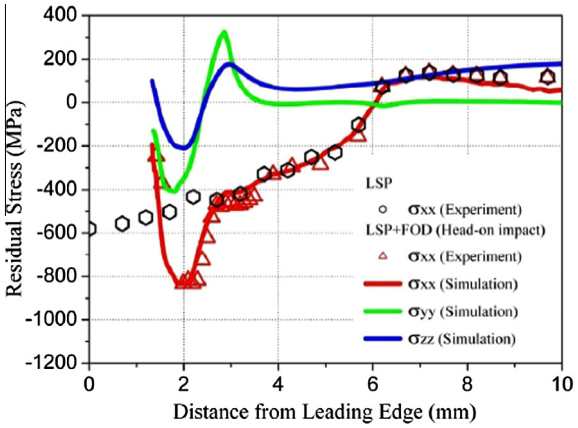

Fig. 6. Comparison of residual stress results from the depth-resolved experiment and the FE simulation on the mid-line mn for head-on impact.

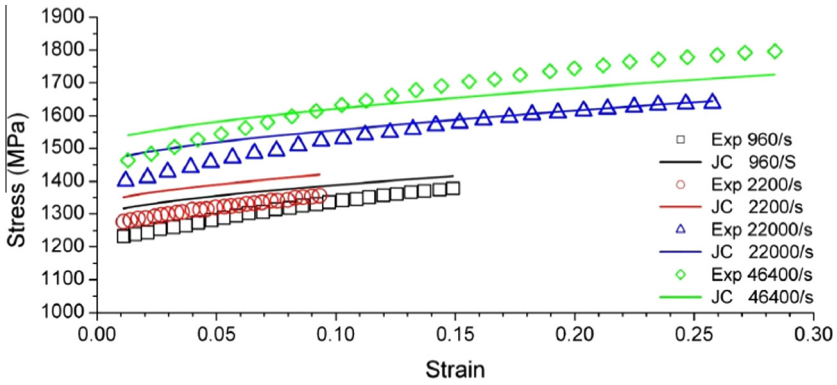

Fig. 7. The stress–strain response as a function of strain rate, comparison of results from Johnson–Cook (JC) constitutive model and the experimental data (Hubert and Meyer, 2006).

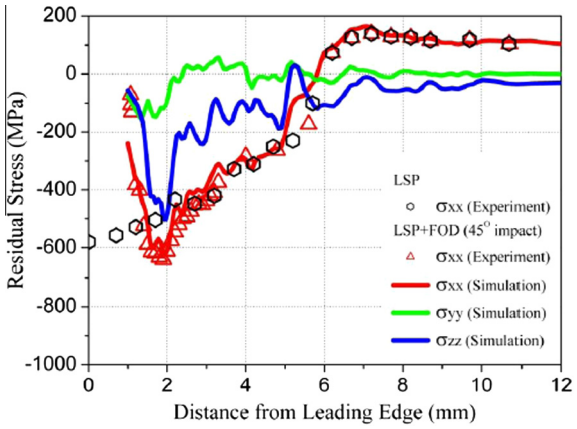

Fig. 8. Comparison of residual stress results from the depth-resolved experiment and the FE simulation on the mid-line mn for 45° impact.

treated sample (Fig. 5), it is clear from both the simulation and the measurements that FOD significantly reduced the compressive stresses near the edge from ~−500 to ~−200 MPa for 0° impact and to −240 (−80 from measurement) MPa for 45° impact, whilst at the same time introducing maximum compressive stresses sub-surface at a distance around 1 mm from the notch tip, about −800 and −650 MPa for head-on and 45° impacts, respectively. While the 0° impact does show a greater compressive stress peak, the stress fields in x-direction from 0° and 45° impacts are rather similar. In both cases the stresses return to those after LSP at a distance about 3 mm from the leading edge.

The effects of FOD impact on the residual stress component σ_{xx} (relevant to crack opening) for head-on and 45° impacts are shown in Fig. 9a and b, respectively. The boundaries of the symmetry plane and the notch post FOD are marked by black lines. For the head-on impact, a "V" notch was predicted along with some material pile-up around the notch due to lateral expansion (refer to A and C in Fig. 9a); for the 45° impact, a notch with a significantly varying depth at the entrance and the exit of the projectile was predicted, although due to the removal of damaged elements during the FE simulation (Fig. 9b), no material pile-up was found in the notch root, consistent with the experimental observations by Spanrad and Tong (2011). The notch depths predicted by the simulations are 1.29 and 0.77 mm for head-on and 45° impacts respectively, which compare favourably with the measured values of 1.43 and 0.78 mm. The contour plots of the residual stress component σ_{xx} after head-on and 45° impacts on LSPed specimens are shown in Fig. 9a and b. Residual stress component σ_{xx} is in the normal direction to the potential crack growth plane, most relevant to crack initiation and growth post FOD impacts following subsequent fatigue loading. Stresses at the center of the notch floor and the crack rim are particular critical for fatigue crack nucleation (Peters and Ritchie, 2000). For head-on impacts, high tensile residual stresses prevail on and near the surface of the specimen, especially in the region of pile-up (marked by A in Fig. 9a) and the on the leading edge next to the notch (marked by B in Fig. 9a), both sources for potential crack onset. By contrast, compressive residual stresses predominate in the interior of the specimen. The results are broadly consistent with the numerical simulation of a rigid sphere impact on the leading edge of a thin blade reported by Chen (2005). For 45° impacts, the results of FE modelling show that whilst large compressive stresses are created around the entrance side of the damage site (marked by A in Fig. 9b), tensile stresses are created and concentrated at the exit side from the impact (marked by B in Fig. 9b). Compared to the 3D stress distribution around the notch due to head-on impacts, it is evident that the tensile stress concentrated in a small local region around the notch in 45° impacts may be particularly detrimental to fatigue resistance and may well serve as preferential sites for fatigue crack nucleation and growth upon the application of cyclic loads. Beyond the immediate vicinity of the notch, the residual stresses become more uniformly distributed through thickness and increasingly compressive over the next millimeter or so and remain compressive to a depth of around 6 mm from the leading edge (i.e. over the entire peened region), beyond which the residual stresses change from compressive to tensile and gradually disappear altogether. This suggests that

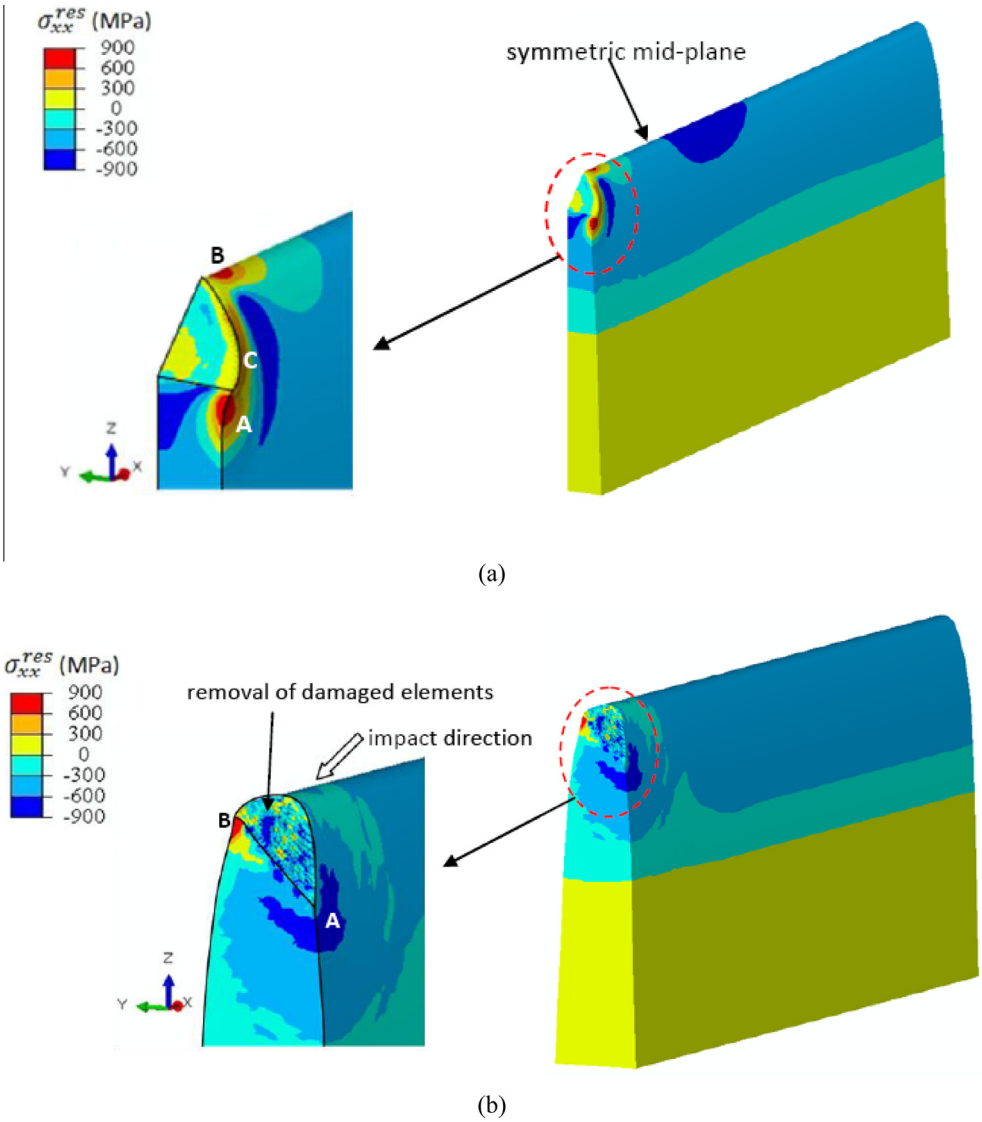

Fig. 9. The residual stress contours for stress component σ_{xx} after (a) head-on impact; (b) 45° impact.

while the local tensile stresses and damage around the notch may aid the nucleation of fatigue cracks, once the crack grows through thickness the compressive residual stresses should effectively impede further fatigue crack growth.

5.3. Residual strain maps

2D maps of residual elastic strains measured by high energy synchrotron X-ray diffraction are compared with the FE predictions. The residual elastic strains are not readily available for visualisation in ABAQUS, so a python script was written to access the ABAQUS output database and to calculate the residual elastic strains, then the computed field outputs were saved to the output database in ABAQUS for visualisation. The predicted 2D residual elastic strain maps on the mid-plane both parallel (longitudinal) to and perpendicular (normal) to the leading edge are compared against the through-thickness measurements and the results are presented in Figs. 10a–10d, respectively. It seems that, overall, the distributions of the experimental and the predicted residual elastic strains around the notch compare reasonably well.

For head-on impacts, Fig. 10a shows the maps of longitudinal residual elastic strain, where a large compressive strain field is observed directly below the notch root, although the distance of the predicted and the experimental peak values to the leading edge differ slightly. Regions of tensile strain are located laterally on the notch flanks. Fig. 10b shows the corresponding map of residual elastic strain normal to the leading edge, where a large tensile residual elastic strain field is observed directly below the notch root. Further tensile strain regions predicted are inconsistent with the measurements, which may be

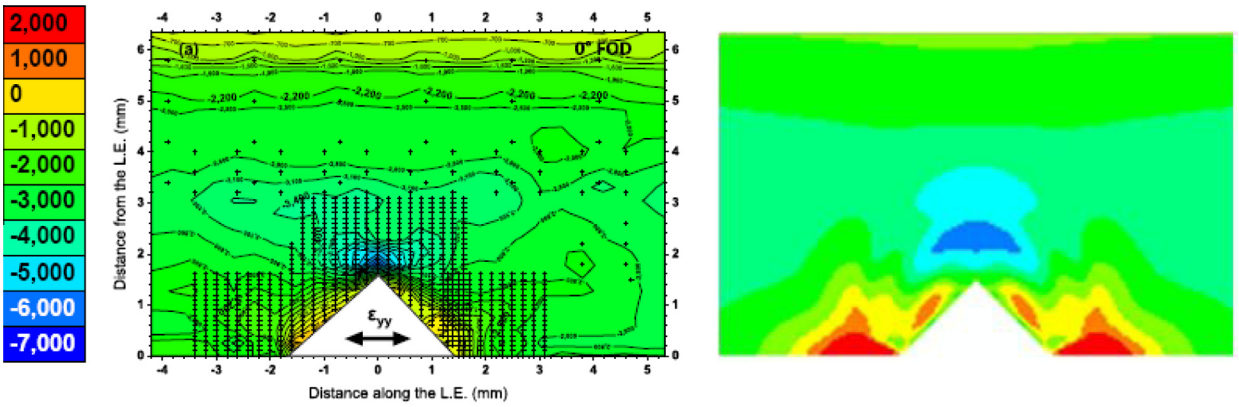

Fig. 10a. The longitudinal residual elastic strain maps for head-on impact from: (a) experimental measurement; (b) FE simulation.

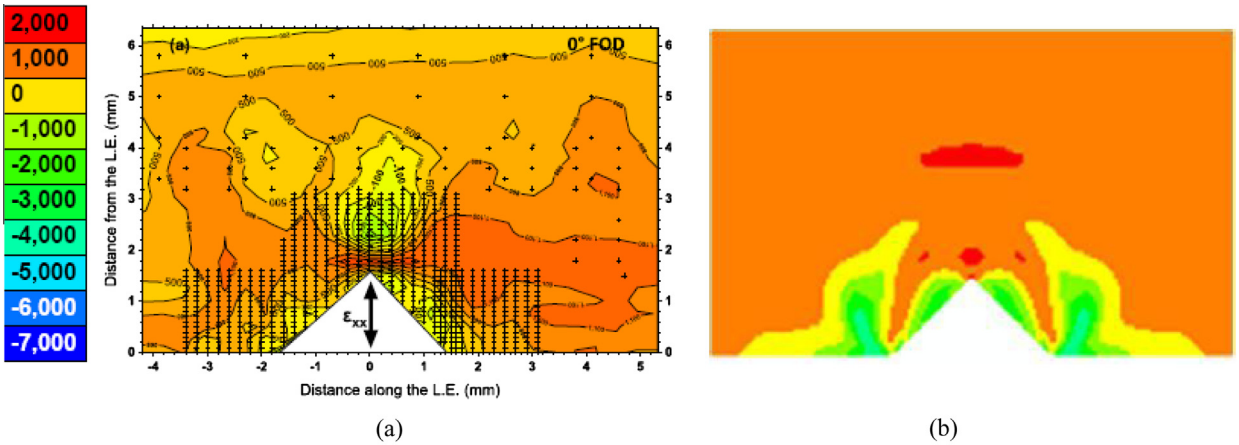

Fig. 10b. Maps of residual elastic strain normal to the leading edge for head-on impact from: (a) experimental measurement; (b) FE simulation.

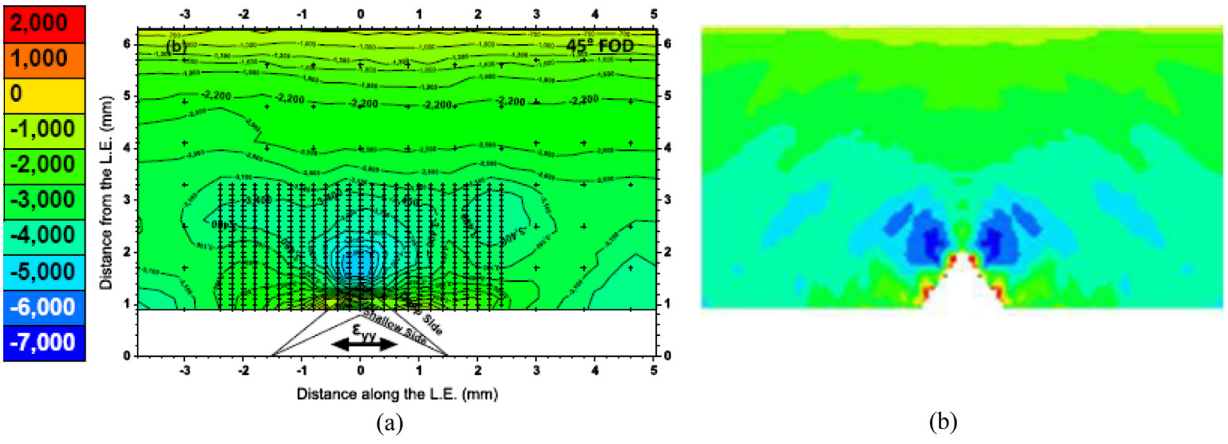

Fig. 10c. The longitudinal residual elastic strain maps for 45° impact from: (a) experimental measurement; (b) FE simulation.

attributed to the neglect of the residual stress σ_{zz} caused by LSP (Fig. 5) in the pre-stress implemented prior to impact simulation. Compressive residual elastic strains are located on the notch flank in Fig. 10b, but the magnitudes of the peak compressive residual elastic strains from the simulation are higher than those from the experiment, which may

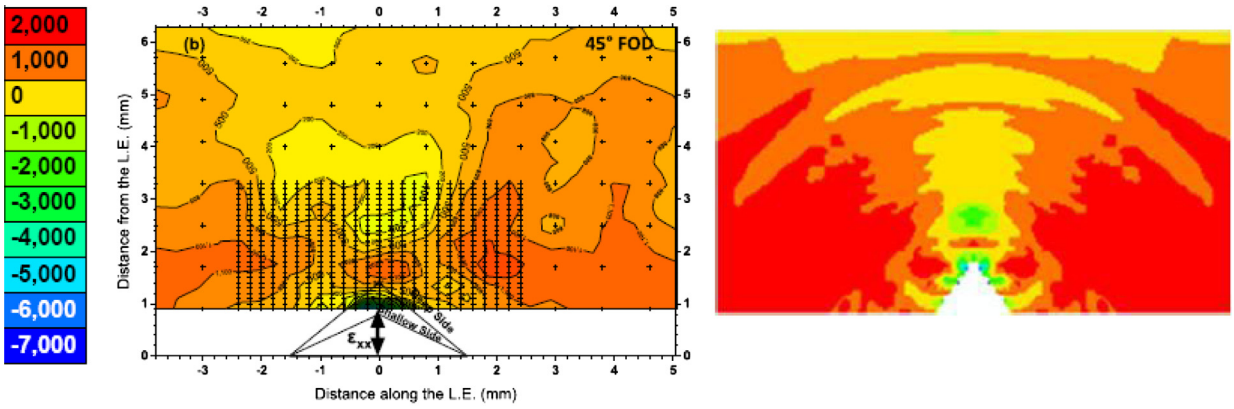

Fig. 10d. Maps of residual elastic strain normal to the leading edge for 45° impact from: (a) experimental measurement; (b) FE simulation.

be due to the fact that the simulation results are values from the symmetric mid-plane (Fig. 9a), whereas the experimental results are through-thickness averages.

For 45° impacts, in which the loss of material is considered in the numerical simulation, 2D maps between the experimental and the predicted residual elastic strains along the longitudinal and normal directions are shown in Figs. 10c and 10d, respectively. Except for a small region of predicted longitudinal tensile residual elastic strains on the notch flank, the distributions of the experimental and the predicted residual stresses are similar, as shown in Figs. 10c and 10d. It should be noted that, although large compressive residual elastic strain regions in longitudinal direction under the notch root are captured by both measurement and FE prediction (Fig. 10c), the distributions differ somewhat with a "fan" type pattern from the FE analysis, as opposed to a "ball" type from the measurement. For the residual strains normal to the leading edge (Fig. 10d), the distributions between the simulation and the measurement are closer.

Overall, the comparisons of the residual strain maps between the experimental and the predicted results are encouraging, considering the difference in the data acquisition: Mid-plane results are presented from the FE analyses, as opposed to average results through the thickness from the measurements. The results also show that the Johnson–Cook material model and its associated failure criterion can provide accurate predictions of the residual elastic strain distributions for head-on and 45° impacts on laser-shock peened Ti–6Al–4V specimens. It is also worth noting that, by comparing the current results with the results for FOD impact on unpeened leading edge geometries (Frankel et al., 2012), the large tensile strained region ahead of the compressive region near the notch in the unpeened sample is absent in the laser peened case, indicating clearly the beneficial effect of LSP treatment.

5.4. Physical damages due to FOD

Experimental studies have been carried out on the damage characterization of aerofoil samples examined here, under head-on and 45° impacts (Spanrad and Tong, 2011). Multiple failure modes were observed, including materials pile-up, folding and fretting debris for head-on impact; and lost of materials by shearing, formation of shear-bands and microcracks for 45° impact. These gave rise to multiple crack initiation sites and prompted accelerated crack growth under simulated service loads, such as low cycle, high cycle and combined low and high cycle fatigue (Lin et al., 2014). Prediction of such crack growth requires considerable confidence in the description of residual stress field due to both surface treatment (LSP) and FOD. The results presented in this paper represent efforts made towards this goal.

6. Conclusions

In this paper, 3D FE models have been developed to simulate the residual stresses/strains due to FOD to the leading edge of a laser-shock peened aerofoil specimen of Ti–6Al–4V alloy. The Johnson–Cook constitutive model with strain-rate hardening and thermal softening terms was used to predict the deformation due to head-on impact; whilst the Johnson–Cook failure criterion was used to predict 45° impact. The following conclusions may be drawn:

(a) Both the mid-line and the mid-plane strain fields from the FE simulation compare reasonably well with the through thickness data from synchrotron diffraction. The Johnson–Cook material model seems to be effective in predicting the dynamic response of laser-shock peened Ti–6Al–4V specimen for head-on and 45° impacts when the associated failure model was incorporated in the latter.
(b) The redistribution of residual stresses due to FOD has been accurately captured in LSPed specimens by the FE simulation. The compressive stresses originally near the leading edge due to LSP are reduced post FOD, although greater compressive stresses now lies around 1 mm from the notch tip.

(c) The 3D full field residual stress contours reveal clearly the position and the magnitude of tensile and compressive residual stresses as well as the deformation around the impact notch. Localised regions of tensile stresses encourage fatigue crack initiation, although the larger compressive stresses ahead of the FOD notch are expected to inhibit further crack growth. These compressive residual stresses were found to vary little even after significant crack growth from the FOD notch (Zabeen, 2012), hence its beneficial effects may continue even in the events of early crack growth.

(d) The region of tensile strain found previously ahead of the compressive strain near the notch for unpeened samples post FOD (Frankel et al., 2012) is absent in the current samples as a result of the compressive stresses due to LSP treatment prior to FOD impacts.

Acknowledgments

The work was funded by the Engineering and Physical Science Research Council (Grants EP/E05658X/1 and EP/E058817/1) and the Ministry of Defence of UK. The advice of Dr Mike Winstone of dstl and Dr John Schofield at Rolls-Royce plc are gratefully acknowledged. The research was carried out in collaboration with Rolls-Royce plc, who provided the LSP treatment of the specimens.

References

Abaqus, 2012. User Manual, Version 6.12, Hibbit, Karsen & Sorensen Inc.
Altenberger, I., Nalla, R.K., Sano, Y., Wagner, L., Ritchie, R.O., 2012. On the effect of deep-rolling and laser-peening on the stress-controlled low- and high-cycle fatigue behavior of Ti–6Al–4V at elevated temperatures up to 550 °C. Int. J. Fatigue 44, 292–302.
Boyce, B.L., Chen, X., Hutchinson, J.W., Ritchie, R.O., 2001. The residual stress state due to a spherical hard-body impact. Mech. Mater. 33 (8), 441–454.
Chen, X., 2005. Foreign object damage on the leading edge of a thin blade. Mech. Mater. 37 (4), 447–457.
Clauer, A.H., Koucky, J.R., 1991. Laser shock processing increases the fatigue life of metal parts. Mater. Process. Rep. 6 (6), 3–5.
Duo, P., Liu, J., Dini, D., Golshan, M., Korsunsky, A.M., 2007. Evaluation and analysis of residual stresses due to foreign object damage. Mech. Mater. 39 (3), 199–211.
Eltobgy, M.S., Ng, E., Elbestawi, M.A., 2004. Three-dimensional elastoplastic finite element model for residual stresses in the shot peening process. Proc. Inst. Mech. Eng. Part B: J. Eng. Manuf. 218, 1471–1481.
Frankel, P.G., Withers, P.J., Preuss, M., Wang, H.-T., Tong, J., Rugg, D., 2012. Residual stress fields after FOD impact on flat and aerofoil-shaped leading edges. Mech. Mater. 55, 130–145.
Hammersley, A.P., Svensson, S.O., Hanfland, M., Fitch, A.N., Hausermann, D., 1996. Two-dimensional detector software: from real detector to idealised image or two-theta scan. High Pressure Res.: Int. J. 14, 235–248.
Hammersley, G., Hackel, L.A., Harris, F., 2000. Surface prestressing to improve fatigue strength of components by laser shot peening. Opt. Lasers Eng. 34 (4–6), 327–337.
Hubert, W., Meyer, J., 2006. A modified Zerilli–Armstrong constitutive model describing the strength and localizing behavior of Ti–6Al–4V. Technical Report ARL-CR-0578: Army Research Laboratory.
Johnson, G.R., Cook, W.H., 1983. A constitutive model and data for metals subjected to large strain, high strain rates, and high temperature. In: Proc. Seventh Int. Symp. Ballistics, The Hague, The Netherlands, pp. 541–547.
Johnson, G.R., Cook, W.H., 1985. Fracture characteristics of three metals subjected to various strains, strain rates, temperatures and pressures. Eng. Fract. Mech. 21 (1), 31–48.
Kay, G., 2003. Failure modeling of titanium 6Al–4V and aluminum 2024-T3 with the Johnson–Cook material model. FAA report, DOT/FAA/AR-03/57 September.
Khan, A.S., Suh, Y.S., Kazmi, R., 2004. Quasi-static and dynamic loading responses and constitutive modeling of titanium alloys. Int. J. Plast. 20 (12), 2233–2248.
King, A., Steuwer, A., Woodward, C., Withers, P.J., 2006. Effects of fatigue and fretting on residual stresses introduced by laser shock peening. Mater. Sci. Eng. A 435–436, 12–18.
Lei, Y., O'Dowd, N.P., Webster, G.A., 2000. Fracture mechanics analysis of a crack in a residual stress field. Int. J. Fract. 106 (3), 195–216.
Lesuer, D.R., 2000. Experimental investigations of material models for Ti–6Al–4V titanium and 2024-T3 aluminum. Final Report: DOT/FAA/AR-00/25, US Department of Transportation, Federal Aviation Administration.
Lin, B., Lupton, C., Spanrad, S., Schofield, J., Tong, J., 2014. Fatigue crack growth in laser-shock-peened Ti–6Al–4V aerofoil specimens due to foreign object damage. Int. J. Fatigue 59, 23–33.
Mannava, S., McDaniel, A.E., Cowie, W.D., Halila, H., Rhoda, J.E., Gutknecht, J.E., 1997. Laser shock peened gas turbine engine fan blade edges. US Patent 5,591,009, General Electric Company (Cincinnati, OH).
Martinez, C.M., Eylon, D., Nicholas, T., Thompson, S.R., Ruschau, J.J., Birkbeck, J., Porter, W.J., 2002. Effects of ballistic impact damage on fatigue crack initiation in Ti–6Al–4V simulated engine blades. Mater. Sci. Eng. A 325 (1–2), 465–477.
Meyer, H.W., Kleponis, D.S., 2001. Modeling the high strain rate behavior of titanium undergoing ballistic impact and penetration. Int. J. Impact Eng 26, 509–521.
MIL-HDBK-5J, 2003. Metallic materials and elements for aerospace vehicle structures, Department of Defense, USA.
Montross, C.S., Wei, T., Ye, L., Clark, G., Mai, Y.W., 2002. Laser shock processing and its effects on microstructure and properties of metal alloys: a review. Int. J. Fatigue 24 (10), 1021–1036.
Nicholas, T., Barber, J.P., Bertke, R.S., 1980. Impact damage on titanium leading edges from small hard objects. Exp. Mech. 20 (10), 357–364.
Nowell, D., 2008. Ballistic simulation of foreign object damage on 20 fatigue specimens. Report: University Technology Centre for Solid Mechanics, University of Oxford.
Nowell, D., Duó, P., Stewart, I.F., 2003. Prediction of fatigue performance in gas turbine blades after foreign object damage. Int. J. Fatigue 25, 963–969.
Peters, J.O., Ritchie, R.O., 2000. Influence of foreign-object damage on crack initiation and early crack growth during high-cycle fatigue of Ti–6Al–4V. Eng. Fract. Mech. 67 (3), 193–207.
Peters, J.O., Roder, O., Boyce, B.L., Thompson, A.W., Ritchie, R.O., 2000. Role of foreign-object damage on thresholds for high-cycle fatigue in Ti–6Al–4V. Metall. Mater. Trans. A 31 (6), 1571–1583.
Peyre, P., Fabbro, R., Merrien, P., Lieurade, H.P., 1996. Laser shock processing of aluminium alloys. Application to high cycle fatigue behaviour. Mater. Sci. Eng. A 210 (1–2), 102–113.
Rankin, Jon E., Hill, Michael R., 2003. Measurement of thickness-average residual stress near the edge of a thin laser peened strip. J. Eng. Mater. Technol. Trans. ASME 125 (3), 283–293.
Ritchie, R.O., Boyce, B.L., Campbell, J.P., Roder, O., Thompson, A.W., Milligan, W.W., 1999. Thresholds for high-cycle fatigue in a turbine engine Ti–6Al–4V alloy. Int. J. Fatigue 21 (7), 653–662.
Ruschau, J.J., John, R., Thompson, S.R., Nicholas, T., 1999. Fatigue crack nucleation and growth rate behavior of laser shock peened titanium. Int. J. Fatigue 21, S199–S209.
Ruschau, J.J., Nicholas, T., Thompson, S.R., 2001. Influence of foreign object damage (FOD) on the fatigue life of simulated Ti–6Al–4V airfoils. Int. J. Impact Eng 25 (3), 233–250.
Ruschau, J., Thompson, S.R., Nicholas, T., 2003. High cycle fatigue limit stresses for airfoils subjected to foreign object damage. Int. J. Fatigue 25 (9–11), 955–962.
Spanrad, S., Tong, J., 2011. Characterisation of foreign object damage (FOD) and early fatigue crack growth in laser shock peened Ti–6Al–4V aerofoil specimens. Mater. Sci. Eng. A 528, 2128–2136.
Turski, M., Clitheroe, S., Evans, A.D., Rodopoulos, C., Hughes, D.J., Withers, P.J., 2010. Engineering the residual stress state and microstructure of stainless steel with mechanical surface treatments. Appl. Phys. A Mater. Sci. Process. 99 (3), 549–556.
Wang, X.M., Shi, J., 2013. Validation of Johnson–Cook plasticity and damage model using impact experiment. Int. J. Impact Eng. 60, 67–75.

Withers, P.J., 2013. Synchrotron X-ray diffraction. In: Schajer, G.S. (Ed.), Practical Residual Stress Measurement Methods. John Wiley & Sons Ltd, pp. 149–176.
Withers, P.J., Preuss, M., Steuwer, A., Pang, J.W.L., 2007. Methods for obtaining the strain-free lattice parameter when using diffraction to determine residual stress. J. Appl. Cryst. 40, 891–904.
Yang, J.-M., Her, Y.C., Han, N., Clauer, A., 2001. Laser shock peening on fatigue behavior of 2024-T3 Al alloy with fastener holes and stopholes. Mater. Sci. Eng. A 298 (1–2), 296–299.
Zabeen, S., 2012. Fatigue crack growth in complex residual stress fields due to surface treatment and foreign object damage under simulated flight cycles (Ph.D. thesis), University of Manchester, UK.
Zabeen, S., Preuss, M., Withers, P.J., 2013. Residual stresses caused by head-on and 45 foreign object damage for a laser shock peened Ti–6Al–4V alloy aerofoil. Mater. Sci. Eng. A 560, 518–527.
Zhang, X.C., Zhang, Y.K., Lu, J.Z., Xuan, F.Z., Wang, Z.D., Tu, S.T., 2010. Improvement of fatigue life of Ti–6Al–4V alloy by laser shock peening. Mater. Sci. Eng. A 527 (15), 3411–3415.